Solution-Processed, Solid-State Solar Cells based on Environmentally Friendly $AgBiS_2$ Nanocrystals

María Bernechea*[,1], Nichole Cates Miller*[,1], Guillem Xercavins[1], David So[1], Alexandros Stavrinadis[1], Gerasimos Konstantatos[1,2]

[1]ICFO-Institut de Ciències Fotòniques, The Barcelona Institute of Science and Technology, 08860 Castelldefels (Barcelona), Spain

[2]ICREA—Institució Catalana de Recerca i Estudis Avançats, Passeig Lluís Companys 23, 08010 Barcelona, Spain

*These authors contributed equally.

Gerasimos.konstantatos@icfo.es

Solution-processed inorganic solar cells are a promising low-cost alternative to first-generation solar cells.[1,2] Solution processing at low temperatures and the use of nontoxic and abundant elements can help minimize cost and facilitate regulatory acceptance. However, until now there has been no material that exhibits all of these features while demonstrating promising efficiencies. Many of the most promising solution-processed inorganic solar cells contain toxic elements such as lead or cadmium (perovskites,[2,3] PbS,[4] CdTe,[5,6] CdS(Se)[7,8]) or scarce elements like tellurium or indium (CdTe, CIGS(Se)/CIS[9,10]). Others require high-temperature processes such as selenization or sintering or rely on vacuum deposition techniques ($Sb_2S(Se)_3$,[11–13] SnS,[14,15] CZTS(Se)[16]). Here, we present $AgBiS_2$ nanocrystals as a novel nontoxic,[17] earth-abundant[18] material for high-performance, solution-processed solar cells fabricated in ambient conditions at low temperatures (≤100°C). The $AgBiS_2$ nanocrystals have favorable properties for solar-cell applications including a near-ideal bandgap and strong, broad absorption. We demonstrate a Newport certified power conversion efficiency of 6.3% with no hysteresis and a remarkably high short-circuit current density of about 22 $mA \cdot cm^{-2}$ for an active layer thickness of only ~35 nm.

Lead-chalcogenide quantum dots[4] stand out among the most promising colloidal nanocrystal materials for solar cells since they are solution-processable and exhibit most of the aforementioned features, although the toxicity of lead remains a concern. On the other hand, $AgBiS_2$, which belongs to the family of I-III-VI_2 compounds, comprises environmentally friendly RoHS-compliant elements. In its nanocrystalline form, $AgBiS_2$ exhibits photoconductivity and favorable thermoelectric properties and has been used as a sensitizer or counter electrode in sensitized solar cells with modest efficiencies.[19–24] Here we present colloidal

$AgBiS_2$ nanocrystals that serve both as the photo-absorbing and charge-transporting medium in high-performance solid-state, solution-processed solar cells.

We have developed a low temperature hot-injection synthetic route for the synthesis of colloidal $AgBiS_2$ nanocrystals (see methods). The nanocrystals are dispersible in most organic solvents, and the solutions are stable for months without nanocrystal precipitation or loss in device performance (Fig. 1a and Supplementary Fig. 1a). As previously reported,[19–24] the material crystallizes in the cubic rock salt structure (Fig. 1b, widening and small deviations in peak positions are due to strain[25]) with nanocrystal diameters of 4.6 ± 1 nm (Fig. 1c). The high-resolution transmission electron micrographs show atomic planes and the fast Fourier transform (FFT) gives d-spacing values of 0.207, 0.316 and 0.287 nm, which correspond to the (220), (111) and (200) interplanar distances of cubic $AgBiS_2$ (Supplementary Fig. 2a), in agreement with the X-ray diffraction (XRD) data. The material exhibits a very high absorption coefficient (10^5 – 10^3 cm^{-1}), comparable to that of CIGS (Supplementary Fig. 2b), with a favorable bandgap of ~1.3 eV (Fig. 1d and Supplementary Fig. 2c).

The as-synthesized $AgBiS_2$ nanocrystals are capped with oleic acid. We therefore sought a ligand exchange that removes oleate ligands to render the deposited films conductive. Following prior work on PbS optoelectronics, ethanedithiol (EDT) was used to replace the oleate ligands and act as a crosslinking molecule.[1,4] X-ray photoelectron spectroscopy (XPS) shows that EDT treatment effectively removes the oleate ligands, since the high-energy components in the Ag 3d and Bi 4f spectra, which are attributed to the bonding of oleic acid in untreated $AgBiS_2$, disappear after EDT treatment (Figs 2a and 2b).[26–28] Effective ligand exchange is further supported by the disappearance of the oleate peaks in the Fourier transform infrared

spectroscopy (FTIR) spectra (Supplementary Fig. 3) and the significant reduction in the amount of oxygen and carbon in the XPS elemental analysis (Fig. 2c).

Solar cells with EDT-treated $AgBiS_2$ active layers were fabricated sandwiched between a ZnO electron transport layer (ETL) and a thin (~10 nm) polymer hole-transport layer (HTL). This structure, shown schematically in Fig. 3a, is similar to the structure employed by Bi_2S_3 n-type nanocrystal solar cells.[29] The polymer layer, which does not contribute to carrier generation (Supplementary Fig. 2d), was intentionally kept thin in order to minimize parasitic absorption. The performance of EDT-treated devices was poor with an average power conversion efficiency of 1.5% (Fig. 2e). To identify the origin of the low performance, we focus on the Bi 4f XPS spectra. After EDT treatment the binding energies of the Bi component (158.1 and 163.4 eV) are higher than those corresponding to elemental bismuth (~157 and ~162 eV). Still, they appear at quite low binding energies relative to standard Bi-S components,[26] thus indicating a high concentration of electrons on the bismuth atoms. This low-energy component was previously observed in the Bi 4f spectra of nanocrystalline Bi_2S_3 films and has been correlated with higher trap density and increased n-type doping.[29] Ultraviolet photoelectron spectroscopy (UPS) also reveals n-type doping in EDT-treated $AgBiS_2$ (Fig. 2d).

We took the view that thiol chemistry may not adequately passivate the $AgBiS_2$ nanocrystals and therefore explored halide chemistry as a more effective passivation scheme.[1,4] Treatment of $AgBiS_2$ nanocrystals with tetramethylammonium iodide (TMAI) resulted in the elimination of the Ag peak associated with Ag-oleate, as was also seen after EDT treatment (Fig. 2a). After TMAI treatment, the Bi 4f component at low binding energies is present, but smaller than observed for the EDT-treated sample (Fig. 2b). The main component, appearing at a high binding energy (~158.7 and ~164.1 eV), can be attributed to Bi-S and Bi-I bonds (the removal of

the original oleic acid is confirmed by FTIR, Supplementary Fig. 3).[30] This shift of the Bi peak to higher binding energies indicates removal of electron density from Bi atoms, pointing to stronger binding with the atomic halide ligands and hence better passivation. TMAI treatment was also found to lead to a more intrinsic semiconductor according to UPS measurements (Fig. 2d) and results in an overall significantly higher average power conversion efficiency of 4.8% (Fig. 2e). The distribution of efficiencies and the average figures of merit for solar cells treated with EDT and TMAI are shown in Supplementary Fig. 5 and Supplementary Table 1, respectively.

It is noteworthy that the presence of both an ETL and a HTL is required in order to achieve high solar-cell performance. Omitting either one of these layers results in significant performance reduction (Supplementary Table 2). To investigate the role of the HTL on device performance, we fabricated TMAI-treated solar cells with a variety of polymer HTLs (Supplementary Fig. 6). The choice of polymer strongly impacts the short-circuit current (J_{SC}), the fill factor (FF), and consequently the solar-cell efficiency. Curiously, the position of the polymer HOMO level has little impact on the open-circuit voltage (V_{OC}) of the devices (Supplementary Table 3), which may indicate that the V_{OC} is limited by trap-assisted recombination. No correlation between the solar-cell figures of merit and the polymer mobility or HOMO level was observed. However, we have observed that thiophene-rich polymers outperform those with few or no thiophene units, indicating that thiophene rings facilitate efficient charge transfer from the $AgBiS_2$ and thus improve charge collection. This is in agreement with results for Sb_2S_3, which has been reported to strongly interact with the thiophene units in polymer HTLs.[11] In addition, the EQE spectrum for the best performing HTL shows a high IR contribution that can only be attributed to $AgBiS_2$, pointing to better charge extraction for the thiophene-rich polymers (Supplementary Fig. 6b).

Optimized TMAI-treated $AgBiS_2$ solar cells exhibit the best performance with a PTB7 HTL. A cross-sectional FIB-SEM image and the approximate energy levels of such a cell are shown in Figs 3b and 3c, respectively. These solar cells exhibit efficiencies up to 5.84% in our lab (Fig. 3d). Initial stability tests indicate promise since these solar cells are stable in air for several weeks (Supplementary Fig. 1b). A particularly striking feature is the high J_{SC} of 18 $mA \cdot cm^{-2}$ despite the small active-layer thickness of ~35 nm. That such high currents can be achieved with such thin active layers highlights the strong absorption of $AgBiS_2$ nanocrystals and their promise as a photovoltaic material in a variety of device structures including tandem and sensitized solar cells.

Fig. 3e shows the external quantum efficiency (EQE) with 1-sun light bias and without light bias. Integration of the 1-sun EQE with the solar spectrum gives a predicted J_{SC} of 17.7 $mA \cdot cm^{-2}$, in good agreement with the observed J_{SC} of 18.0 $mA \cdot cm^{-2}$. However, the J_{SC} predicted for the EQE *without* light bias is higher (20.2 $mA \cdot cm^{-2}$). To better understand this, in Fig. 3f we show how the $AgBiS_2$-layer thickness affects observed J_{SC}, J_{SC} from EQE without light bias, and J_{SC} calculated with transfer-matrix-model (TMM) simulations assuming 100% internal quantum efficiency. The TMM-simulated J_{SC} exhibits three regions that are labeled in the figure: (1) an increase with increasing thickness below ~40 nm, (2) a dip around 100 nm due to optical interference effects, and (3) a second increase at higher thicknesses. The J_{SC} from EQE without light bias shows this same trend and exhibits current densities that approach the simulated values. Because the TMM simulation assumes complete collection of all excited charges, these results indicate that charge collection is efficient at low light intensities. On the other hand, the observed J_{SC} values, which are from measurements at 1 sun, drop off for high thicknesses; this demonstrates that current collection is less efficient at higher light intensities in devices thicker

than 50 nm. These results suggest that an intensity-dependent process is responsible for current loss, particularly in solar cells with thick $AgBiS_2$ layers.

To further investigate this, we also measured J_{SC} and V_{OC} as a function of light intensity. The dependence of J_{SC} on light intensity in Fig. 4a is fitted with a power-law expression ($J_{SC} \propto Intensity^{\alpha}$) where $\alpha = 0.88$. This nonlinearity ($\alpha \neq 1$) is caused by incomplete extraction of charges prior to recombination.[31] Fig. 4b shows V_{OC} as a function of light intensity. The fit gives an ideality factor of 1.3, which indicates Shockley-Read-Hall (SRH) trap-assisted recombination.[32] Improvements to the ligand-exchange process or the use of alternative surface passivation schemes should further suppress trap-assisted recombination and increase solar-cell performance. We also performed transient photovoltage (TPV) measurements with light biases ranging from about 0.2 to 1 sun and fit the photovoltage decays to determine carrier lifetime (τ) as a function of V_{OC} (Fig. 4c). As expected, carrier lifetime decreases with increasing light intensity (and increasing V_{OC}). The carrier lifetime at 1 sun is ~2 μs, on par with that of PbS quantum dot solar cells.[33] We hypothesize therefore that current losses in thicker $AgBiS_2$ devices is due to poor carrier transport. Further improvements to the synthesis and the ligand exchange should be sought to increase and balance charge transport.

To corroborate our findings we sent devices to Newport for independent certification (see Supplementary Fig. 7). In Fig. 5, we present the Newport-certified results of a record-performing device with an efficiency of 6.3% and an impressive J_{SC} of 22 $mA \cdot cm^{-2}$ (Fig. 5 and Supplementary Fig. 7). $AgBiS_2$ solar cells do not exhibit hysteresis when the voltage is scanned in the forward and reverse directions (Fig. 5a). The light-biased EQE spectrum demonstrates strong photocurrent response in the favorable region of 300-1100 nm (Fig. 5b). This certified

result further demonstrates the promise of $AgBiS_2$ as a highly absorbing, solution-processed material for photovoltaic applications.

In conclusion, we have presented a new class of ultrathin-film solution-processed colloidal nanocrystal solar cells based on $AgBiS_2$ nanocrystals with power conversion efficiencies up to 6.3%. To our knowledge, this is the first efficient inorganic solar material that simultaneously meets demands for nontoxicity, abundance, and low-temperature solution processing. $AgBiS_2$ nanocrystals also have significant potential as ultrathin absorbing layers in other device architectures such as sensitized and tandem solar cells due to the high J_{SC} of our devices (up to 22 $mA \cdot cm^{-2}$) despite their very thin active layers (~35 nm). Furthermore, better nanocrystal passivation, light-trapping schemes, and nanostructuring[34,35] of the active layer should help overcome the limitations of these devices and result in efficiencies beyond the already compelling ones reported herein.

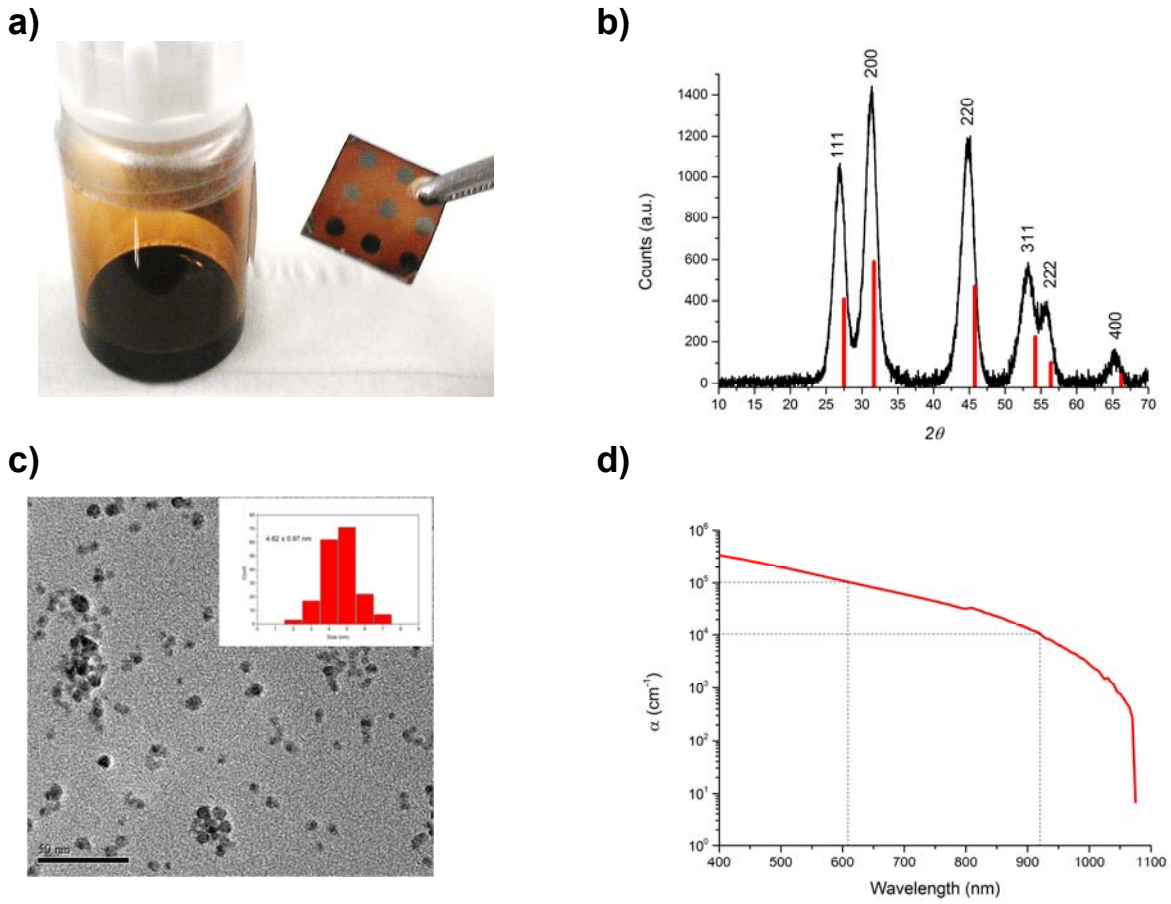

Figure 1: $AgBiS_2$ properties. (a) Picture of a vial containing an $AgBiS_2$ solution in toluene and a solar cell made with it. (b) XRD pattern of $AgBiS_2$ and reference pattern for cubic $AgBiS_2$ (Ref.: 00-004-0699), confirming the rock salt structure. (c) TEM micrograph of $AgBiS_2$ nanocrystals (scale 50 nm). Inset, size distribution histogram. (d) Absorption coefficient measurement on solid state films of $AgBiS_2$ nanocrystals.

a) **b)**

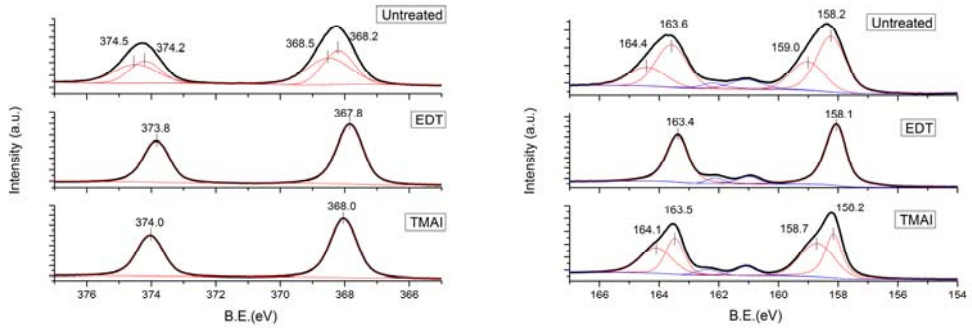

c)

Sample	Ag	C	O	S (2s)	I
Untreated	1.5	12.5	1.9	1.6	
EDT	1.3	2.5	0.3	2.1	
TMAI	1.4	3.0	0.9	1.6	0.8

[a)]Quantities normalized to bismuth

d) **e)**

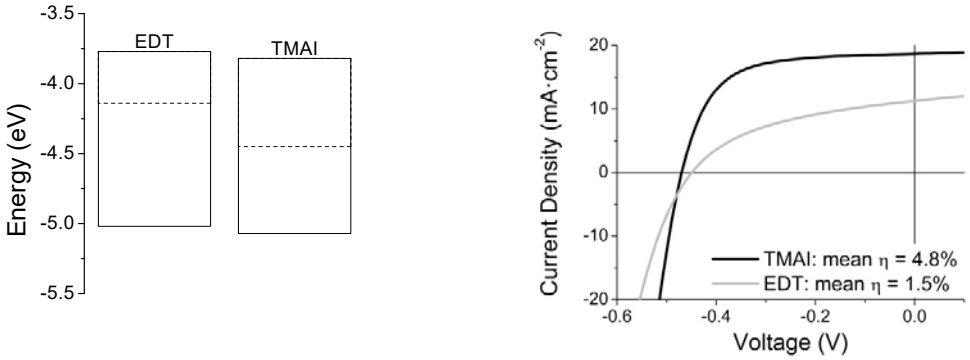

Figure 2: XPS core-level spectra of (a) Ag 3d and (b) Bi 4f and S 2p for the untreated and ligand-exchanged samples. (c) Relative amounts of each element found by XPS (d) Energy levels as determined by UPS for $AgBiS_2$ after ligand exchange with EDT and TMAI. Measurement details are given in Supplementary Fig. 4. (e) J-V curves for solar cells treated with TMAI and EDT along with the mean efficiency (η) obtained for each. A histogram showing the distribution of efficiencies for EDT- and TMAI- treated solar cells and the average figures of merit are shown in Supplementary Fig. 5 and Supplementary Table 1, respectively.

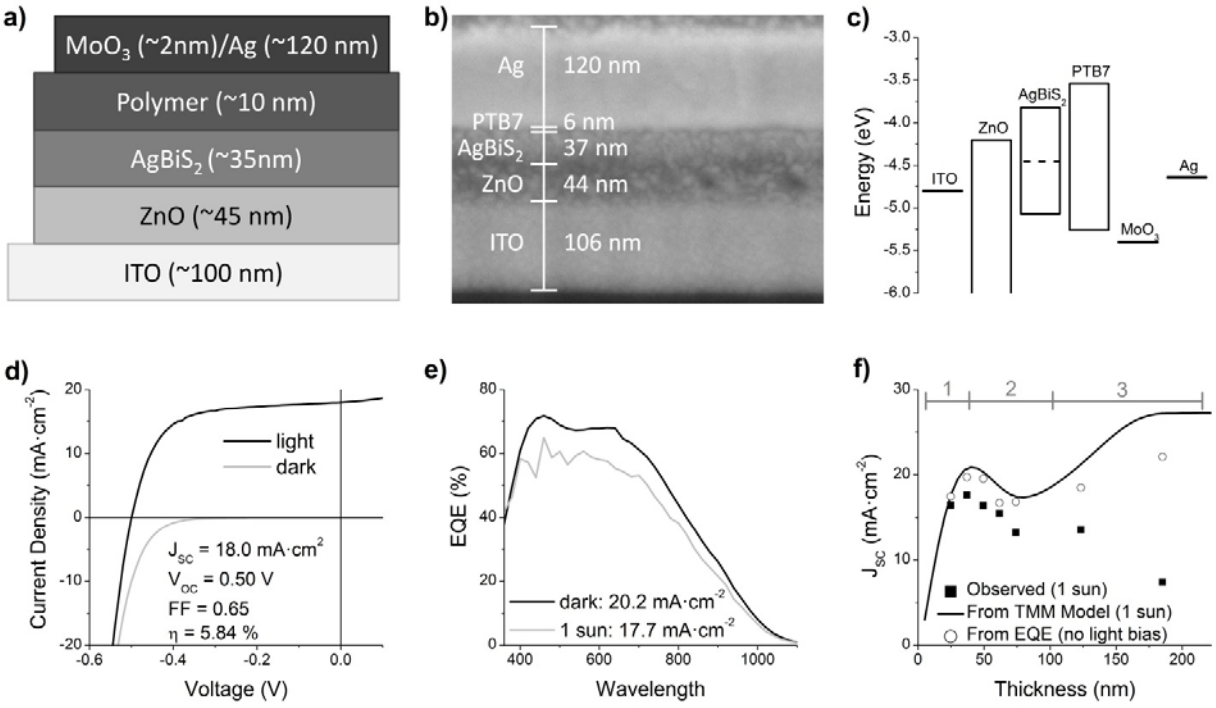

Figure 3: (a) Structure of $AgBiS_2$ solar cells. (b) FIB-SEM image of device cross section. (c) Approximate energy levels of solar-cell materials. (d) J-V curves of best solar-cell device. (e) EQE without light bias and with 1-sun light bias. (f) Observed J_{SC} values from J-V measurements at 1 sun (filled squares), J_{SC} values calculated from TMM simulations (line), and J_{SC} values predicted from EQE without light bias (open circles), as a function of $AgBiS_2$ thickness.

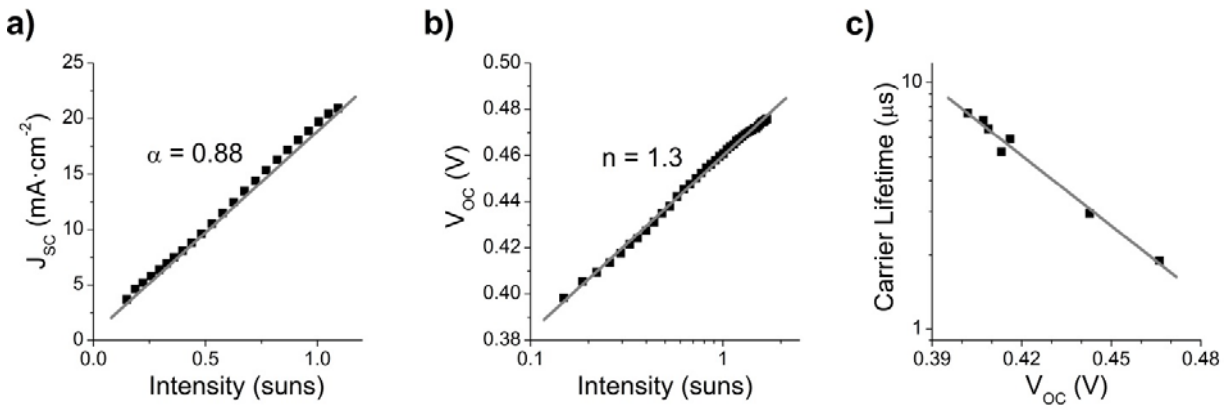

Figure 4: (a) J_{SC} and (b) V_{OC} as a function of the light intensity. (c) Carrier lifetimes extracted from TPV measurements as a function of V_{OC}.

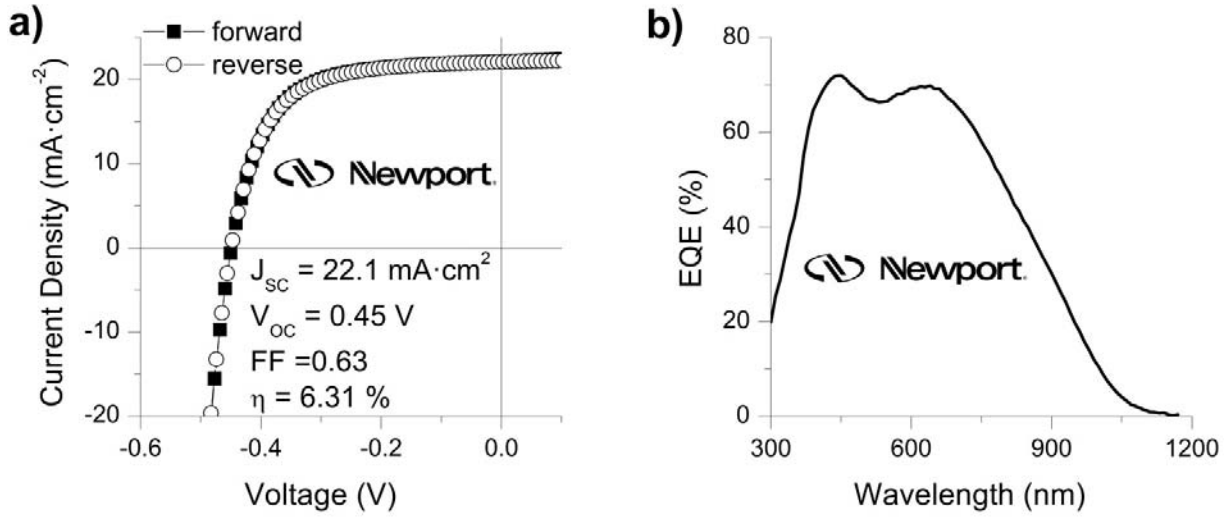

Figure 5: Newport-certified (a) J-V and (b) light-biased EQE curves. Supplementary Fig. 7 shows the accreditation certificate.

Acknowledgements

The authors thank Johann Osmond for ellipsometry measurements and Helmut Maeckel for developing the TMM simulation code and device-characterization setups. The research leading to these results has received funding from Fundació Privada Cellex, and European Community's Seventh Framework program (FP7-ENERGY.2012.10.2.1) under grant agreement 308997. We also acknowledge financial support from the Spanish Ministry of Economy and Competitiveness (MINECO) and the "Fondo Europeo de Desarrollo Regional" (FEDER) through grant MAT2014-56210-R. This work was also supported by AGAUR under the SGR grant (2014SGR1548). N.C.M acknowledges support by Marie Curie Actions - FP7-PEOPLE-2013-IIF (Project Number: 622358). G.K. acknowledges financial support from the Spanish Ministry of Economy and Competitiveness, through the "Severo Ochoa" Programme for Centres of Excellence in R&D (SEV-2015-0522).

Author contributions

M.B. conceived, synthesized and characterized the material, and co-wrote the manuscript. N.C.M. fabricated and characterized devices, ran and analyzed TMM simulations, designed experiments, and co-wrote the manuscript. G.X. and D.S. fabricated and characterized devices. A.S. took the FIB-SEM image. G.K. supervised the work, directed the study and co-wrote the manuscript. All authors discussed the results, have read and agreed to the publication of this manuscript.

Additional information

Supplementary information is available in the online version of the paper. Reprints and permissions information is available online at www.nature.com/reprints.

Correspondence and request for materials should be adressed to G.K.

Competing financial interests

The authors declare no competing financial interests.

Methods

Chemicals and Materials

All the reactions were carried out using standard Schlenk techniques. Reagents were purchased from Sigma Aldrich, except $Bi(OAc)_3$ which was purchased from Alfa Aesar. PTB7 (poly[(4,8-bis-(2-ethylhexyloxy)-benzo(1,2-b:4,5-b′)dithiophene)-2,6-diyl-alt-(4-(2-ethylhexyl)-3-fluorothieno[3,4-b]thiophene-)-2-carboxylate-2-6-diyl)]) and PCE-10 (poly[4,8-bis(5-(2-ethylhexyl)thiophen-2-yl)benzo[1,2-b;4,5-b']dithiophene-2,6-diyl-alt-(4-(2-ethylhexyl)-3-fluorothieno[3,4-b]thiophene-)-2-carboxylate-2-6-diyl)]) were purchased from 1-material, P3HT (poly(3-hexylthiophene-2,5-diyl) was purchased from Rieke Metals, PEDOT:PSS (poly(3,4-ethylenedioxythiophene) polystyrene sulfonate) was purchased from Heraeus Clevios, and Spiro-OMeTAD (2,2',7,7'-Tetrakis-(N,N-di-4-methoxyphenylamino)-9,9'-spirobifluorene) from Merk.

Synthesis of $AgBiS_2$ Nanocrystals

For the synthesis of $AgBiS_2$ nanocrystals 1 mmol of $Bi(OAc)_3$, 0.8 mmol of Ag(OAc) and 17 mmol of oleic acid (OA) were pumped overnight at 100ºC to form the bismuth and silver oleates and remove oxygen and moisture. After this time the reaction atmosphere was switched to Ar and 1 mmol of HMS (hexamethyldisilathiane) dissolved in 5 ml of ODE (1-octadecene) was quickly injected to the flask while the heating was stopped (without removing the heating mantel) and the reaction was allowed to cool down slowly. The nanocrystals were isolated after the addition of acetone and centrifugation, purified by successive dispersion in toluene and precipitation with acetone and finally dispersed in anhydrous toluene. The reaction flasks were protected from light until precipitation.

Characterization of $AgBiS_2$ Nanocrystals

UV-Vis absorption measurements were performed using a Cary 5000 UV-VIS-NIR spectrophotometer in solution on a glass cuvette of 1 mm optical path or as films on glass substrates. For the absorption coefficient measurements, an integrating sphere setup was used. Films exchanged with TMAI were grown on glass, the thickness was measured using a profilometer, and then the absorption coefficient was determined as described elsewhere.[36]

Transmission electron microscopy (TEM) and X-Ray diffraction (XRD) measurements were performed in the Scientific and Technological Centres of the University of Barcelona (CCiT-UB).

TEM micrographs were obtained using a JEOL 2100 microscope operating at an accelerating voltage of 200 kV. Samples were prepared by placing two drops of a diluted toluene solution on a holey carbon-coated grid and allowing the solvent to evaporate in air. The average diameter was calculated by measuring the diameters of no less than 100 nanocrystals from non-aggregated areas.

XRD data were collected using a PANalytical X'Pert PRO MPD Alpha1 powder diffractometer in Bragg-Brentano $\theta/2\theta$ geometry of 240 millimeters of radius, Cu Kα radiation: λ = 1.5406 Å and work power: 45 kV – 40 mA.

UV photoelectron spectroscopy (UPS) and X-ray photoelectron spectroscopy (XPS) measurements were performed at the Institut Català de Nanociencia i Nanotecnologia (ICN2).

XPS measurements were performed with a Phoibos 150 analyzer (SPECS GmbH, Berlin, Germany) in ultra-high vacuum conditions (base pressure 1E-10 mbar) with a monochromatic Kalpha X-ray source (1486.74eV). The pass energy values used was 10 eV for the high resolution spectrum and the energy resolution as measured by the FWHM of the Ag 3d5/2 peak for a sputtered silver foil was 0.55 eV. Intensities were estimated by calculating the integral of each peak, determined by subtracting the Shirley-type background and fitting the experimental curve to a combination of Lorentzian and Gaussian lines of variable proportions. Accurate binding energies (0.2eV) were determined by referencing to the C 1s peak at 284.8 eV. UPS measurements were performed on a SPECS PHOIBOS 150 electron spectrometer using the monochromated HeI radiation (21.2 eV). Samples were prepared by covering ITO substrates (approximately 10 x 10 mm) with the toluene solutions and allowing the solvent to evaporate in air, or following a layer-by-layer process as described in the solar cell fabricationsection.

Fourier transform infrared spectroscopy (FTIR) measurements were performed on a Cary 600 FTIR spectrophotometer in transmission mode using Nujol mulls between polyethylene sheets.

Solar-Cell Fabrication

All solar-cell fabrication steps were performed in air. ITO-covered glass substrates (Universität Stuttgart, Institut für Großflächige Mikroelektronik) were cleaned by ultrasonicating in soapy water, acetone, and isopropanol for 10 minutes each and dried with nitrogen. A ~45-nm ZnO layer was then grown using a sol-gel method. 1 g of zinc acetate dihydrate was dissolved in 10 mL of methoxyethanol and 284 μL of ethanolamine. The solution was spin cast onto the ITO-covered glass substrates at 3000 rpm and heated at 200°C for 30 minutes. This process was then

repeated to insure uniform coverage of ZnO on the ITO. Afterwards, a ~35-nm film of $AgBiS_2$ nanocrystals was deposited using three rounds of a layer-by-layer (LBL) process using a 20 mg/mL solution of $AgBiS_2$ in toluene filtered through a 0.45 μm polytetrafluoroethylene (PTFE) filter. One LBL cycle involves dropping one drop of the $AgBiS_2$ solution onto the ZnO-covered substrate spinning at 2000 rpm and waiting 10 seconds, adding five drops of TMAI (1 mg/mL in methanol) or EDT (2% in acetonitrile) and waiting 20 seconds. For TMAI, this step was repeated once with an additional five drops of the TMAI solution and an additional 20 seconds of waiting. The TMAI- and EDT-treated films were then rinsed with either methanol or acetonitrile, respectively, and then rinsed with toluene. For thinner and thicker $AgBiS_2$ layers, more or fewer cycles of the LBL process were performed. After the $AgBiS_2$ deposition, the TMAI- and EDT-treated samples were annealed in air for 10 minutes at 100°C and 50°C, respectively. The samples were then stored in air in the dark overnight before depositing a thin layer of PTB7 by spin coating a 5 mg/mL solution of PTB7 in dicholorobenzene at 2000 rpm. Finally, a Kurt J. Lesker Nano36 system was used to evaporate 2 nm of MoO_3 and 120 nm of Ag through a shadow mask to produce solar cells with a diameter of 2 mm (area of 3.1 mm^2) . The devices were kept in air in the dark for at least one day before measuring.

Solar-Cell Characterization

All device characterization was performed in air at ambient conditions. Current-voltage measurements were performed with a Keithley 2400 source meter and a Newport Oriel Sol3A solar simulator with an AM1.5 filter. The intensity of the solar simulator was adjusted using a Hamamatsu S1336 silicon photodiode that was calibrated at the Fraunhofer Institute of Solar Energy Systems, Freiburg, Germany.

The external quantum efficiency (EQE) was measured using a Newport Cornerstone 260 monochromator, a Thorlabs MC2000 chopper, a Stanford Research SR570 transimpedance amplifier, and a Stanford Research SR830 lock-in amplifier. A calibrated Newport 818-UV photodetector was used as a reference. Light bias was provided by a Newport xenon arc lamp.

Measurements of the J_{SC} and V_{OC} as a function of light intensity were performed with an Agilent 4000X oscilloscope with a 50 Ω and 1 MΩ input terminal, respectively. A FiberTech Optica LED lightsource provided the bias light.

Transient photovoltage (TPV) measurements were performed with an Agilent 4000X oscilloscope using a 1 MΩ input terminal and a Vortran Stradus laser with a wavelength of 637 nm. A FiberTech Optica LED lightsource provided the bias light. Carrier lifetimes (τ) and V_{OC} were determined by fitting the exponential photovoltage decays with $V = A\exp\left(-\frac{t}{\tau}\right) + V_{OC}$ where V is the photovoltage, A is an exponential prefactor, and t is time.

The cross section of the device was imaged using an in-lens secondary electron detector of a Zeiss Auriga FIB-SEM microscope operated at 5 kV. The cross section was prepared in situ by depositing a thin (a few nanometers) layer of Pt atop the device via a gas injection system integrated in the microscope and subsequently using the FIB mode of the microscope to mill down a 6 µm x 2 µm rectangular region of the top surface.

References

1. Kramer, I. J. & Sargent, E. H. The architecture of colloidal quantum dot solar cells: materials to devices. *Chem. Rev.* **114,** 863–82 (2014).
2. Kazim, S., Nazeeruddin, M. K., Grätzel, M. & Ahmad, S. Perovskite as light harvester: a game changer in photovoltaics. *Angew. Chem. Int. Ed. Engl.* **53,** 2812–24 (2014).
3. Zhou, H. *et al.* Interface engineering of highly efficient perovskite solar cells. *Science* **345,** 542–546 (2014).
4. Chuang, C. M., Brown, P. R., Bulović, V. & Bawendi, M. G. Improved performance and stability in quantum dot solar cells through band alignment engineering. *Nat. Mater.* **13,** 796–801 (2014).
5. Major, J. D., Treharne, R. E., Phillips, L. J. & Durose, K. A low-cost non-toxic post-growth activation step for CdTe solar cells. *Nature* **511,** 334–337 (2014).
6. Panthani, M. G. *et al.* High efficiency solution processed sintered CdTe nanocrystal solar cells: The role of interfaces. *Nano Lett.* **14,** 670–675 (2014).
7. Santra, P. K. & Kamat, P. V. Mn-doped quantum dot sensitized solar cells: A strategy to boost efficiency over 5%. *J. Am. Chem. Soc.* **134,** 2508–2511 (2012).
8. Pan, Z. *et al.* Near infrared absorption of CdSe(x)Te(1-x) alloyed quantum dot sensitized solar cells with more than 6% efficiency and high stability. *ACS Nano* **7,** 5215–5222 (2013).
9. Reinhard, P. *et al.* Review of Progress Toward 20% Efficiency Flexible CIGS Solar Cells and Manufacturing Issues of Solar Modules. *IEEE J. Photovoltaics* **3,** 572–580 (2013).
10. Romanyuk, Y. E. *et al.* All Solution-Processed Chalcogenide Solar Cells - from Single Functional Layers Towards a 13.8% Efficient CIGS Device. *Adv. Funct. Mater.* **25,** 12–27 (2015).
11. Im, S. H. *et al.* Toward Interaction of Sensitizer and Functional Moieties in Hole-Transporting Materials for Efficient Semiconductor-Sensitized Solar Cells. *Nano Lett.* **11,** 4789–4793 (2011).
12. Chang, J. A. *et al.* Panchromatic Photon-Harvesting by Hole-Conducting Materials in Inorganic–Organic Heterojunction Sensitized-Solar Cell through the Formation of Nanostructured Electron Channels. *Nano Lett.* **12,** 1863–1867 (2012).
13. Zhou, Y. *et al.* Thin-film Sb2Se3 photovoltaics with oriented one-dimensional ribbons and benign grain boundaries. *Nat. Photonics* **9,** 409–415 (2015).
14. Steinmann, V. *et al.* 3.88% Efficient Tin Sulfide Solar Cells using Congruent Thermal Evaporation. *Adv. Mater.* **26,** 7488–7492 (2014).
15. Sinsermsuksakul, P. *et al.* Overcoming efficiency limitations of SnS-based solar cells. *Adv. Energy Mater.* **4,** 1400496–02 (2014).
16. Kim, J. *et al.* High Efficiency Cu2ZnSn(S,Se)4 Solar Cells by Applying a Double In2S3/CdS Emitter. *Adv. Mater.* **26,** 7427–7431 (2014).

17. Mohan, R. Green bismuth. *Nat Chem* **2,** 336 (2010).

18. Vesborg, P. C. K. & Jaramillo, T. F. Addressing the terawatt challenge: scalability in the supply of chemical elements for renewable energy. *RSC Adv.* **2,** 7933 (2012).

19. Liang, N. *et al.* Homogenously hexagonal prismatic AgBiS2 nanocrystals: controlled synthesis and application in quantum dot-sensitized solar cells. *CrystEngComm* **17,** 1902–1905 (2015).

20. Huang, P., Yang, W. & Lee, M. AgBiS2 Semiconductor-Sensitized Solar Cells. *J. Phys. Chem. C* **117,** 18308–18314 (2013).

21. Pejova, B., Grozdanov, I., Nesheva, D. & Petrova, A. Size-dependent properties of sonochemically synthesized three-dimensional arrays of close-packed semiconducting AgBiS2 quantum dots. *Chem. Mater.* **20,** 2551–2565 (2008).

22. Pejova, B., Nesheva, D., Aneva, Z. & Petrova, A. Photoconductivity and relaxation dynamics in sonochemically synthesized assemblies of AgBiS2 quantum dots. *J. Phys. Chem. C* **115,** 37–46 (2011).

23. Guin, S. N. & Biswas, K. Cation disorder and bond anharmonicity optimize the thermoelectric properties in kinetically stabilized rocksalt AgBiS2 nanocrystals. *Chem. Mater.* **25,** 3225–3231 (2013).

24. Chen, C., Qiu, X., Ji, S., Jia, C. & Ye, C. The synthesis of monodispersed AgBiS2 quantum dots with a giant dielectric constant. *CrystEngComm* **15,** 7644 (2013).

25. Qin, W., Nagase, T., Umakoshi, Y. & Szpunar, J. A. Relationship between microstrain and lattice parameter change in nanocrystalline materials. *Philos. Mag. Lett.* **88,** 169–179 (2008).

26. Malakooti, R. *et al.* Shape-Controlled Bi2S3 Nanocrystals and Their Plasma Polymerization into Flexible Films. *Adv. Mater.* **18,** 2189–2194 (2006).

27. Krsmanovi, R. *et al.* Colloids and Surfaces B : Biointerfaces Adsorption of sulfur onto a surface of silver nanoparticles stabilized with sago starch biopolymer. *Colloids Surfaces B Biointerfaces* **73,** 30–35 (2009).

28. Dong, T. *et al.* One-step synthesis of uniform silver nanoparticles capped by saturated decanoate : direct spray printing ink to form metallic silver films. *Phys. Chem. Chem. Phys.* **11,** 6269–6275 (2009).

29. Bernechea, M., Cao, Y. & Konstantatos, G. Size and bandgap tunability in Bi 2 S 3 colloidal nanocrystals and its effect in solution processed solar cells. *J. Mater. Chem. A* **3,** 20642–20648 (2015).

30. Boopathi, K. M. *et al.* Solution-processable bismuth iodide nanosheets as hole transport layers for organic solar cells. *Sol. Energy Mater. Sol. Cells* **121,** 35–41 (2014).

31. Cowan, S. R., Roy, A. & Heeger, A. J. Recombination in polymer-fullerene bulk heterojunction solar cells. *Phys. Rev. B* **82,** 245207 (2010).

32. Kirchartz, T., Deledalle, F., Tuladhar, P. S., Durrant, J. R. & Nelson, J. On the differences between dark and light ideality factor in polymer:Fullerene solar cells. *J. Phys. Chem.*

Lett. **4,** 2371–2376 (2013).

33. Chuang, C.-H. M. *et al.* Open-Circuit Voltage Deficit, Radiative Sub-Bandgap States, and Prospects in Quantum Dot Solar Cells. *Nano Lett.* 150430101741001 (2015). doi:10.1021/acs.nanolett.5b00513

34. Rath, A. K., Bernechea, M., Martinez, L. & Konstantatos, G. Solution-Processed Heterojunction Solar Cells Based on p-type PbS Quantum Dots and n-type Bi2S3 Nanocrystals. *Adv. Mater.* **23,** 3712–3717 (2011).

35. Rath, A. K. *et al.* Solution-processed inorganic bulk nano-heterojunctions and their application to solar cells. *Nat. Photonics* **6,** 529 –534 (2012).

36. Martino, M. C. and A. P. C. and M. Realistic absorption coefficient of ultrathin films. *J. Opt.* **14,** 105701 (2012).